



HAL
open science

Growth of Ultrathin Well-Defined and Crystalline Films of Co₃O₄ and CoOOH by Electrodeposition

Ivan Pacheco, Mathilde Bouvier, O M Magnussen, Fouad Maroun, Philippe Allongue

► **To cite this version:**

Ivan Pacheco, Mathilde Bouvier, O M Magnussen, Fouad Maroun, Philippe Allongue. Growth of Ultrathin Well-Defined and Crystalline Films of Co₃O₄ and CoOOH by Electrodeposition. Journal of The Electrochemical Society, 2023, 170 (1), pp.012501. 10.1149/1945-7111/acafaa . hal-04540689

HAL Id: hal-04540689

<https://hal.science/hal-04540689>

Submitted on 10 Apr 2024

HAL is a multi-disciplinary open access archive for the deposit and dissemination of scientific research documents, whether they are published or not. The documents may come from teaching and research institutions in France or abroad, or from public or private research centers.

L'archive ouverte pluridisciplinaire **HAL**, est destinée au dépôt et à la diffusion de documents scientifiques de niveau recherche, publiés ou non, émanant des établissements d'enseignement et de recherche français ou étrangers, des laboratoires publics ou privés.

Growth of ultrathin well-defined and crystalline films of Co_3O_4 and CoOOH by electrodeposition

I. Pacheco¹, M. Bouvier¹, O. M. Magnussen^{2*}, P. Allongue^{1*}, F. Maroun^{1*}

¹ Laboratoire de Physique de la Matière Condensée (PMC), CNRS, Ecole Polytechnique, Institut Polytechnique de Paris, 91120 Palaiseau, France

² Institut für Experimentelle und Angewandte Physik, Christian-Albrechts-Universität zu Kiel, Kiel, Germany.

* *corresponding authors:*

fouad.maroun@polytechnique.edu, philippe.allongue@polytechnique.edu,
magnussen@physik.uni-kiel.de

Abstract

Cobalt oxides are among the best noble metal free catalysts for the oxygen evolution reaction in alkaline electrolyte. To elucidate the origin of their catalytic properties, crystalline films with well-defined orientation and surface quality are needed. In this work, we study the growth of ultrathin crystalline films of cobalt oxides layers on Au(111). The films are grown by electrodeposition at reflux temperature in cobalt nitrate alkaline solutions in the presence of tartrate. The film structure and morphology is studied by X-ray diffraction, atomic force microscopy and scanning electron microscopy, as a function of the deposition parameters (solution composition, potential). Single phase $\text{Co}_3\text{O}_4(111)$ and $\text{CoOOH}(001)$ films in epitaxy with the Au(111) substrate could be obtained by choosing the conditions of deposition. The CoOOH films present a smooth morphology with several 100 nm wide pyramidal islands with stepped facets. The morphology of Co_3O_4 films consists of three-dimensional densely packed triangular islands with flat tops. Finally, we investigate the influence of the substrate on the morphology of Co_3O_4 films by depositing them on Au(100) and a CoOOH buffer layer. The nucleation and growth modes as well as the reaction mechanisms are discussed.

1. Introduction

It has been shown since decades, both experimentally [1] and theoretically [2], that transition metal oxides are among the best catalysts for water oxidation. The quest for scalable solution for sustainable energy conversion triggered a large number of studies in designing and synthesizing such oxides [3] [4] [5] [6] [7] [8] [9]. Among those, cobalt-oxides and their alloys have received a special attention since they can be synthesized by different routes and they offer a large flexibility to tune their activity for oxygen evolution reaction (OER) in alkaline electrolytes [3] [10].

Cobalt oxides can be prepared using chemical routes. Co_3O_4 was for instance prepared by thermal salt decomposition [11], autoclave [12] or sol-gel synthesis [13]. In the case of CoOOH , solvothermal synthesis often generates films composed of micrometric flakes [14]. Cobalt oxides were also synthesized using electrochemical methods. The electrodeposition of $\text{Co}(\text{OH})_2$ allows preparing Co_3O_4 films after oxidation, either by post-aging or by controlled anodic oxidation of the initial deposit [5] [15,16,17]. Koza et al. reported the direct electrodeposition of Co_3O_4 films [18]. Here, $\text{Co}(\text{II})$ oxidation at reflux temperature in an alkaline $\text{Co}(\text{NO}_3)_2$ solution containing sodium tartrate as stabilizing agent, results in the growth of compact and well crystallized Co_3O_4 films on different substrates. Similarly, the anodic deposition of crystallized CoOOH films was reported by electrochemical oxidation of a $\text{Co}(\text{II})$ salt (nitrate or chloride) in solutions of pH 7 to 12 [19] [20] [21]. Depending on the deposition temperature, the morphology of the deposits may be compact or composed of an assembly of nanoflakes. Other Co oxide phases have been also grown electrochemically. The well-known CoCat, which is reputed to be among the best OER catalyst, was for instance prepared by direct electrochemical oxidation of $\text{Co}(\text{NO}_3)_2$ in 0.1 M potassium phosphate (pH 7) [22][18,23] [24]. The CoCat differs however from above cobalt oxides because it is amorphous and contains a significant amount of solution species, such as phosphates.

The above synthesis routes yield very often oxides with amorphous, polycrystalline or nanocrystalline structure and a complex morphology with a large electrochemically active surface area (ECSA). However, benchmarking catalysts requires a standard methodology to determine the ECSA allowing a proper OER current normalization [5] [25] [26]. In this context, model catalysts such as single crystal electrodes or two dimensional epitaxial films appear as a very interesting approach to establish clear structure – OER reactivity relationships, since the ECSA may be measured by scanning probe microscopy and the surface is composed of limited types of active sites, determined by the surface crystallographic orientation.

Model catalysts may be prepared by electrochemical methods. For instance, in ref. [18] epitaxial $\text{Co}_3\text{O}_4(111)$ films were electrodeposited on a single crystal electrode Au(111). We demonstrated recently that 2D and compact epitaxial CoOOH films may be electrodeposited on Au(111) [27]. Furthermore, single crystal oxide electrodes [28] or two-dimensional epitaxial oxide films [29] [30] [31] may also be prepared under ultrahigh vacuum (UHV) conditions.

In this work, we study the nucleation and growth modes of CoOOH(001) and $\text{Co}_3\text{O}_4(111)$ epitaxial films electrodeposited on Au(111). These films have been used in our recent *operando* structural studies in OER conditions [27] [32]. Our study focuses on the growth of thin films (thickness < 40 nm) deposited at reflux temperature in potentiostatic conditions from a diluted cobalt nitrate alkaline solution in the presence of tartrate. We investigate the influence of the deposition parameters, in particular the NaOH and $\text{Co}(\text{NO}_3)_2$ concentrations, and the deposition potential as well as the substrate. The film structure and morphology are characterized using X ray diffraction, atomic force microscopy and scanning electron microscopy. The nucleation and growth modes of the different cobalt oxides are discussed and the reaction mechanisms leading to their formation is briefly addressed.

2. Experimental

The gold substrate were hat-shaped Au(111) single crystals (MaTeck) with an orientation uncertainty of $< 0.1^\circ$. The diameter of the polished (111) surface is 4 mm. Cobalt(II) nitrate hexahydrate ($\geq 99.0\%$), L-(+)-tartaric acid ($\geq 99.5\%$), sodium hydroxide ($\geq 98.0\%$, pellets), potassium sulphate ($\geq 99.0\%$ purity), were purchased from SIGMA-ALDRICH and used as received. Sulphuric acid (96%), and hydrogen peroxide (30%) were purchased from Carlo Erba and used as received. All solutions were prepared using ultrapure Milli-Q water (18.2 M Ω ·cm).

Prior to oxide film preparation, the Au crystal was immersed in a hot 1:2 mixture of 30% H₂O₂ and 96% H₂SO₄ (both Carlo Erba, RSE) for 1 minute to remove any remaining oxide from previous experiments and then annealed in a butane flame for 5 minutes.

Deposition of the oxide was performed on Au(111) at reflux temperature (~ 101 - 106°C depending on the NaOH concentration) in an oxygen-free solution of 0.1 to 1 mM Co(NO₃)₂ + sodium tartrate (tart) in 1 to 5 M NaOH. The sodium tartrate concentration was 1.2 times the concentration of Co(NO₃)₂. At these temperatures, the electrolyte is boiling inducing large convection in the deposition cell even though the sample is standstill. No other forced convection methods were used. Potential control was established using a Pt wire as counter electrode and a Mercury Sulphate Electrode (MSE) reference electrode. The reference electrode was installed in a separate compartment containing potassium sulphate 0.1 M and was connected to the cell using a Teflon capillary. Oxide deposition consists in electrooxidizing the solution at a fixed potential (in the range -0.55 to -0.3 V_{MSE}). The current density in this potential range was 0.1-0.4 mA/cm². These electrodeposition conditions are close to those reported in Ref. [18]. However, to grow very thin films, the electrochemical

charge was smaller in our case (2-20 mC/cm²). After the film preparation, the sample was rinsed with Milli-Q water, dried with Ar and stored in air for further characterizations.

A direct correlation between the deposition charge and the average film thickness d_{av} could not be established. For films covering entirely the gold surface, we considered that d_{av} equals the average crystallite height d_{\perp} determined by X-ray diffraction (see next paragraph). For films with incomplete surface coverage, we determined d_{av} by multiplying d_{\perp} by the coverage determined from microscopy images. After deposition, the samples were quickly removed from the reflux cell, rinsed with ultrapure water, dried with Ar.

The structure of the deposits was determined by X-ray diffraction using a Rigaku SmartLab X-ray diffractometer with a copper rotating anode and a Ge(220)x2 monochromator (K α 1 with a $\lambda = 1.5406\text{\AA}$ and $E = 8.048\text{keV}$). The average crystallite height d_{\perp} was derived from theta-2theta scans and calculated from the Scherrer formula:

$$d_{\perp} = \frac{0.9 \times \lambda}{\text{FWHM}(2\theta) \times \cos \theta} \quad (1)$$

where theta is the Bragg angle and FWHM(2theta) is the full width at half maximum of the Bragg peak in 2theta. The epitaxial relationship of the deposit with the substrate was determined from phi scan (sample rotation angle around its surface normal) measured with a beam incident angle of 0.6° and the detector height and azimuth angles defining the Bragg conditions.

The morphology of deposits was characterized by an Agilent 5500 atomic force microscope (AFM) in non-contact mode and a Hitachi S4800 scanning electron microscope (SEM). Silicon AFM tips with a cantilever oscillating frequency of ~170 kHz (*umasch*) were used. AFM images were flattened using a polynomial with an order of 1 or 2, using the SPIP software (Image Metrology). The SEM was operated at 3 to 10kV.

3. Results

Figure 1 presents the X ray diffraction (XRD) scans in the theta-2theta configuration of different Co oxide films on Au(111) (samples 1, 2 and 3 in **Table 1**) prepared in a solution containing 1 mM $\text{Co}(\text{NO}_3)_2$ and 1.2 mM Sodium tartrate with different NaOH concentrations. The detailed deposition conditions are given in **Table 1**. In the long range scans of **Fig. 1a**, in addition to the Au(111) peaks indicated by black dashed lines, one observes two sets of peaks, marked in red and blue. The red diffraction peaks at 19° and 59.3° may be indexed as (111) and (333) planes, respectively, of face centred cubic (fcc) Co_3O_4 . $\text{Co}_3\text{O}_4(222)$ and $\text{Co}_3\text{O}_4(444)$ are not visible because they are hidden by the intense Au(111) and Au(222) peaks. The peaks marked in blue can be assigned to hexagonal CoOOH , with the peaks at $20^\circ, 40.8^\circ, 62.9^\circ$ and 88.2° corresponding to the (003), (006), (009), and (0012) Bragg reflections, respectively. For films prepared in 1 M NaOH (sample 1) only the Co_3O_4 peaks are found, indicating that the oxide film is composed of a single phase with a single crystallographic orientation, i.e., $\text{Co}_3\text{O}_4(111)$. Films prepared in 5 M NaOH (sample 3) exhibit only the CoOOH peaks, indicating a $\text{CoOOH}(001)$ deposit. These results are corroborated by our previous surface X-ray diffraction studies [27] [32]. A mixture of both oxide phases is formed in 2M NaOH (sample 2). **Fig. 1b** shows the first order diffraction peaks in more detail. For the film grown in 5 M NaOH, it evidences two satellite peaks (indicated by blue arrows) sitting on each side of the $\text{CoOOH}(003)$ peak. They are separated from the centre of the main peak by $\sim 0.6^\circ$. These satellite peaks are Laue fringes. Their measured separation from the Bragg peak corresponds to what is expected, i.e., 1.5 times the peak's full width at half maximum (FWHM) [33]. Similarly to the FWHM, the position of these fringes allows also to determine the average crystallite height. Most importantly, the presence of these fringes indicates that the CoOOH film is flat and that its thickness is homogeneous over the sample area probed by the X ray beam. Such fringes are absent for the other deposits, in particular for the

Co₃O₄(111) deposit grown in 1 M NaOH. This is related to the large crystallites height distribution.

Table 1: Influence of the deposition conditions (electrolyte concentration and deposition potential) on the oxide phase electrodeposited on Au(111) .

Sample	[NaOH]	[Co(tart)]	Deposition potential	Deposition charge	Oxide phase (d_{\perp} in nm)
1	1 M	1 mM	-0.55 V	10 mC/cm ²	Co ₃ O ₄ (30.7)
2	2 M	1 mM	-0.5 V	8 mC/cm ²	Co ₃ O ₄ (17.5) + CoOOH (33.2)
3	5 M	1 mM	-0.5 V	10 mC/cm ²	CoOOH (21.5)
4	1 M	0.5 mM	-0.55 V	4 mC/cm ²	Co ₃ O ₄ (14.2)+ CoOOH (30)
5	1 M	0.1 mM	-0.55 V	2 mC/cm ²	CoOOH (23.9)
6	1 M	1 mM	-0.4 V	8 mC/cm ²	Co ₃ O ₄ (20.5)
7	1 M	1 mM	-0.3 V	8 mC/cm ²	Co ₃ O ₄ (20.3)

Quantitative analysis of the Bragg peaks provides further structural details on the films. The average crystallite height (d_{\perp}), given in **Table 1**, was estimated from the first order peak full width half maximum (FWHM) using Eq. 1 in the experimental section. The positions of the CoOOH(003) peak and its higher order peaks are clearly smaller than those of bulk CoOOH indicating a significant out-of-plane strain of $\epsilon_{\perp} = +1.1 \pm 0.1\%$. In the case of the Co₃O₄(111) and Co₃O₄(333) peaks, the shift corresponds to a strain of only $\epsilon_{\perp} = -0.15 \pm 0.05\%$. When both phases are present in the film (sample 2), the CoOOH strain is similar to that of a single phase film whereas the Co₃O₄ strain amounts to $-0.6 \pm 0.2\%$. It is also worth noticing that in this case d_{\perp} is different for the two phases: 33.2 nm for CoOOH and 17.5 nm for Co₃O₄. **Table 2** summarizes the values of ϵ_{\perp} and the in-plane strain ϵ_{\parallel} (taken

from Ref [32]) as well as the expected in-plane lattice mismatch between the oxide films and the substrate using lattice parameters found in the literature of bulk Co oxides ($a = b = 0.572$ nm, $c = 1.4$ nm for Co_3O_4 and $a = b = 0.285$ nm, $c = 1.315$ nm for CoOOH). In the last line of the **Table 2**, the substrate is a $\text{CoOOH}(001)$ buffer layer deposited on $\text{Au}(111)$ under the same conditions as above (see last part of the Results section). ϵ_{\parallel} and ϵ_{\perp} are negligible for Co_3O_4 . On the other hand, in the case of CoOOH , one notices a significant in-plane tensile strain, and a significant elongation of the CoOOH lattice along the c -axis. This lattice expansion in all directions cannot be due to elastic deformation. It possibly arises from intercalation of species from the electrolyte (possibly water molecules) between layers of OCoO entities along the (001) direction which interact exclusively via H bonds.

Table 2: In-plane lattice mismatch and strains (ϵ_{\perp} out-of-plane and ϵ_{\parallel} in-plane) of cobalt oxide layers electrodeposited on various substrates. The in plane lattice parameters are: $a_{\text{Au}} = 0.2884$ nm, $a_{\text{CoOOH}} = 0.2851$ nm and $a_{\text{Co}_3\text{O}_4} = 0.5716$ nm.

oxide	Substrate	In-plane Mismatch (%) ^{a)}	ϵ_{\perp} (%)	ϵ_{\parallel} (%) ^{b)}
CoOOH(001)	Au(111)	-1.1	+1.1	+0.75
Co ₃ O ₄ (111)	Au(111)	-0.9	-0.15	-0.21
Co ₃ O ₄ (111)	CoOOH(001)	-1 ^{c)}	-0.26	

a) The mismatch is calculated as $(a_{\text{dep}} - a_{\text{sub}})/a_{\text{sub}}$ for CoOOH and $(a_{\text{dep}} - 2a_{\text{sub}})/2a_{\text{sub}}$ for Co₃O₄, with a_{sub} and a_{dep} being the in-plane lattice distance of the substrate and the deposit, respectively, according to values in the literature. In the case of Co₃O₄, we use $2a_{\text{sub}}$ in the formula because the Co₃O₄ lattice parameter is very close to twice that of Au.

b) Taken from Ref [32]

c) Value estimated with respect to the expanded in-plane lattice parameter of the CoOOH buffer layer on Au(111)

The in-plane orientation of the crystallites was characterized by performing phi scans of the sample at specific Bragg conditions (see experimental section). **Figure 2** shows such phi scans for CoOOH(015) (**Fig. 2a**) and Co₃O₄(151) (**Fig. 2b**), together with scans for Au(-111) Bragg conditions which serves as a reference for the phi angle. The Au(-111) scans (black curves) exhibits 3 peaks separated by 120° which is consistent with the 3-fold symmetry of this family of planes. We observe 6 peaks of similar amplitudes for CoOOH(015) (**Fig. 2a**, red curve), which is expected from the hexagonal symmetry around the CoOOH(001) orientation. In between these peaks the intensity is negligible, indicating that the film has one well-defined in-plane orientation. The average separation $\Delta\Phi_1$ between CoOOH and Au peaks amounts to 14.8°, which is significantly lower than the theoretical value (15.17°) but equals

the expected value for an epitaxial CoOOH(001) film with 1% strain along the c axis. We can thus conclude that the CoOOH films are in epitaxy with the Au(111) substrate, with the epitaxial relationship CoOOH(001)[100]//Au(111)[11-2]. This is consistent with previous reports [27].

In the case of Co₃O₄(151) (**Fig. 2b**), 6 peaks of similar amplitudes positioned every 60° are observed, with negligible intensity between the peaks. Since only 3 peaks are expected for this plane's orientation, the Co₃O₄ crystallites have to adopt two in-plane orientations separated by 180°, each yielding 3 peaks. The average separation $\Delta\Phi_2$ between Co₃O₄ and Au peaks amounts 29.33°, which is very close to the theoretical value of 29.4°. We conclude that the Co₃O₄ films are formed of crystallites in epitaxy with the Au(111) substrate adopting the epitaxial relationships Co₃O₄(111)[1-10]//Au(111)[1-10] and Co₃O₄(111)[1-10]//Au(111)[-110] with equal probability. In addition, for each in-plane orientation, the Co₃O₄ lattice is aligned with that of the Au substrate. Again, this is consistent with previous reports [27].

The average FWHM of the CoOOH and Co₃O₄ peaks equals to $\sim 1.4^\circ \pm 0.1^\circ$ and $\sim 1.9^\circ \pm 0.2^\circ$, respectively, which is significantly larger than that of the Au peaks ($\sim 0.4^\circ$) and the instrumental broadening (0.25°). This peak broadening is significantly larger than that expected from the crystallite lateral size, indicating an in-plane orientation distribution of the crystallites of $\sim 1^\circ$ around their preferred orientations along the densely packed atomic directions of Au(111) (see analysis of discussion in supporting information, section S7). This is consistent with a small lattice strain within the Co oxide films.

The morphology of the films is presented by the AFM images in **Fig. 3** where d_{av} is indicated in nm in the top right corner of the images. For these films the coverage is close to 1 and $d_{av} \sim d_{\perp}$. In the case of Co₃O₄ (**Fig. 3a**), the oxide film has a granular morphology, covering the entire Au surface with a lateral island size between 30 nm and 100 nm. The flat morphology of the Au(111) substrate surface is presented in the supporting information for

comparison (**Fig. S1**). Most of the Co_3O_4 islands have straight edges and many present a clear triangular shape (examples are highlighted with triangles in **Fig. 3a**). The triangular shape is consistent with the (111) symmetry of the cubic spinel structure of the Co_3O_4 spinel phase. The triangle edges must be parallel to dense directions belonging to the $\langle 1-10 \rangle$ or $\langle 11-2 \rangle$ families. The grain orientations are equally distributed along two opposite directions indicated by the red and blue drawn triangles, in agreement with the two families of three Bragg peaks in the phi scan of **Fig. 2b**. The height profile shown in **Fig. 3d** exhibits variations in the range ± 4 nm. However, the top of the islands is flat, with a height fluctuation within ± 0.5 nm. The latter corresponds to approximately four times the height difference between two Co planes of the oxide along the (111) direction (0.23 nm).

By comparison, Co_3O_4 films also grow (111) on Au(100) and present two populations of islands as shown in the AFM images of **Fig. S2** for $d_{\text{av}} = 15$ nm. The largest islands are preferentially located along straight lines which are approximately orthogonal whereas the smallest islands are present almost everywhere. The distribution of these lines and their separation by several tens of nm is consistent with the atomic step distribution on the Au(100) surface. We may thus conclude that on this surface, we have a preferential nucleation of Co_3O_4 islands along the substrate steps. It is not clear why such preferential nucleation was not observed on Au(111) steps.

The topography of the CoOOH film is smoother. In **Fig. 3b**, we observe shallow pyramidal islands of 2-4 nm in height (see **Fig. 3e**). These islands have a very large triangular base (indicated exemplarily by white triangles), with typical lateral size ranging from 100 nm to 500 nm. The pyramid facets exhibit regularly spaced atomic steps with a constant facet angle of $\sim 2^\circ$, independent of the pyramid size. Steps are also visible in height profiles as the one shown in **Fig. 3e**, where a single step is highlighted by two red arrows. The measured step height is ca. 0.4-0.5 nm which is close to the distance between two Co planes along the c axis

of CoOOH (0.44 nm) and is consistent with previous reports [27]. At the top of some of the CoOOH islands, we could evidence the presence of a screw dislocation (**Fig. S3a-b**), but in other cases, we could not find any (**Fig. S3c-d**). The average height of the pyramids, i.e., the height difference between its top and the bottom determined from the AFM images is significantly smaller than $d_{\perp} = 14$ nm. This suggests that the pyramidal islands are sitting on a 2D CoOOH layer and that the growth of CoOOH(001) is rather two dimensional. This is also supported by AFM images of thinner CoOOH films (see below).

In the case where both oxide phases coexist, two distinct characteristic morphologies are observed in the AFM images (**Fig. 3c**) and the corresponding height profiles (**Fig. 3f**). One morphology consists of triangular islands with an average lateral size ~ 50 nm and two 180° rotated in-plane orientations, similar to what is observed for pure Co_3O_4 films. They may therefore be assigned to $\text{Co}_3\text{O}_4(111)$. In other places the topography of the deposit in **Fig. 3c** consists of large shallow islands which are similar to that of the CoOOH(001) film in **Fig. 3b**. For both types of islands, the island height in the AFM images reaches up to 20 nm, which is close to the value of d_{\perp} obtained by XRD ($d_{\perp} = 14$ nm for CoOOH and $d_{\perp} = 18$ nm for Co_3O_4). We can thus conclude that both phases grow directly on the Au(111) substrate, rather than one phase growing on top of the other.

Figures 4a-c present SEM images of Co_3O_4 films on Au(111) with increasing d_{av} (see experimental section). All films are grown at -0.55 V in a solution containing 1 mM $\text{Co}(\text{NO}_3)_2$ and 1.2 mM sodium tartrate in 1 M NaOH. For $d_{\text{av}} = 5$ nm (**Fig. 4a**), the film is composed of separated islands with $d_{\perp} = 16$ nm. They cover $\sim 30\%$ of the Au surface and their density is around $900 \mu\text{m}^{-2}$. All grains have a triangular shape with two opposite preferred orientations, including the smallest ones (see inset of **Fig. 4a**). The lateral grain size distribution is broad and extends from 7 nm to 35 nm with an average value of $19 \text{ nm} \pm 5 \text{ nm}$ (see the size distribution in supporting information **Fig. S4**). For $d_{\text{av}} = 19$ nm, the islands are tightly

packed and have an average lateral size of 42 nm (see **Fig. S4**). For $d_{av} = 40$ nm (**Fig. 4c**), the average lateral island size increases to 70 nm. The values in the last two cases are an underestimation, because they were calculated using well separated individual islands only, whereas larger islands composed of several coalesced islands were not considered.

Figure 4d shows the CoOOH morphology after depositing a few CoOOH monolayers on Au(111) at -0.55 V in a solution containing 1 mM $\text{Co}(\text{NO}_3)_2$, 1.2 mM sodium tartrate and 5 M NaOH. In the lower part of this AFM image, two bare Au terraces separated by an atomic step are present. In the upper part of the image, the Au terraces are covered by CoOOH with large atomically flat regions which are several 100 nm wide and which height is 1-4 times that of a CoOOH atomic layer. This is shown in the line profile in **Fig. 4e** taken along the dashed line in the image. At 0.1 μm , a ~ 0.25 nm high step is found, which is consistent with the expected 0.235 nm height of atomic steps on Au(111), whereas the height of the deposit's step (at 0.27 and 0.52 μm) is ~ 0.45 nm, corresponding to the spacing between the Co planes in CoOOH(001). The local CoOOH layer thickness is indicated in **Fig. 4e** where the underlying Au step morphology is schematized by the blue line. The CoOOH morphology in this low d_{av} range is following that of the Au substrate, which is a clear signature of a layer-by-layer growth. For both $d_{av} = 8$ nm (**Fig. 4e**) and $d_{av} = 18$ nm (**Fig. S5a**), the morphology is very similar to the one observed in **Fig. 3b**. The main noticeable change is an increase of the average island size with increasing d_{av} : the islands size is in the range 50-500 nm for $d_{av} = 8$ nm and close to 800 nm for $d_{av} = 18$ nm. One may also observe, in the latter case, that at some locations, an abrupt step of several nm is observed in the cross section in **Fig. S5b** (indicated by a red arrow).

In the following, we will describe the influence of the deposition parameters ($\text{Co}(\text{NO}_3)_2$ concentration, the deposition potential, the substrate) on the oxide film structure and morphology. **Fig. 5** presents XRD spectra of two films deposited with 0.1 mM (curve a) and

0.5 mM (curve b) $\text{Co}(\text{NO}_3)_2$ (the concentration ratio of sodium tartrate to $\text{Co}(\text{NO}_3)_2$ is 1.2 in both cases). In the first case, only the Bragg peak corresponding to CoOOH phase is found. At a concentration of 0.5 mM, both phases are present in the film, as indicated by the presence of Co_3O_4 and CoOOH Bragg peaks.

Fig. 6 presents AFM images of three deposits prepared in 1 M NaOH + 1 mM $\text{Co}(\text{NO}_3)_2$ at different potentials, -0.55, -0.40, and -0.30 V. In all three cases, the resulting thickness $d_{\text{av}} \sim 20$ nm and the deposition time were similar indicating that the deposition rate does not vary significantly in this potential range. The three films are continuous and consist of a single phase Co_3O_4 (111). The main difference between the deposits is a decrease of the lateral island size and a corresponding increase of the island density at more positive deposition potentials. The triangular shape of the islands is maintained at -0.4 V. For the deposit grown at -0.3 V, the island shape determination is more difficult, because of the small grain size and the finite size of the AFM tip.

Finally, we also studied the growth of Co_3O_4 on a $\text{CoOOH}(001)$ buffer layer on Au(111). The $\text{CoOOH}(001)$ was electrodeposited employing the conditions of **Figs. 1** and **3b** and is covering the entire Au surface. Subsequently, Co_3O_4 was deposited in a second step from 1 M NaOH + 1 mM $\text{Co}(\text{NO}_3)_2$ + 1.2 mM sodium tartrate electrolyte. The corresponding theta-2theta scan exhibits peaks at the position expected for the CoOOH film (black curve in **Fig. S6**). After Co_3O_4 deposition, the CoOOH peak is still visible with a similar intensity and an additional Co_3O_4 peak appears (**Fig. S3**, red line). The structure of the deposit is therefore a double layer $\text{Co}_3\text{O}_4(111)/\text{CoOOH}(001)$.

Figure 7 compares SEM images of these $\text{Co}_3\text{O}_4/\text{CoOOH}$ films on Au(111) with that of pure Co_3O_4 films for $d_{\text{av}} = 35 - 40$ nm. In both cases, the Co_3O_4 film covers the substrate entirely. However, the granular morphology of the films is clearly different: the typical triangular islands of Co_3O_4 on Au(111) (< 100 nm lateral size) are still present even at this

large thickness whereas, on CoOOH, they have merged to form larger islands (up to several 100 nm lateral size) with undefined shape. This suggests that the Co₃O₄(111) film grows smoother on CoOOH(001) than on Au(111).

4. Discussion

This section is divided in two parts, discussing, first, the reaction mechanism and, second, the nucleation and growth mode. The reaction mechanism below has been proposed by Switzer and co-workers [18] to explain the electrodeposition of Co₃O₄:



The first reaction (**1a**) is the only electrochemical step and produces Co³⁺ species that are completely insoluble in alkaline electrolyte. The second one (**1b**) is a precipitation reaction in which a Co²⁺(tartrate) decomplexation and Co²⁺ and Co³⁺ co-precipitation take place. If we assume that reaction (**1a**) is also the first step for CoOOH formation, the second step would be the following precipitation reaction where only Co³⁺ species are involved:



Both precipitation reactions are expected to take place on the electrode surface and not in the solution bulk since the Co³⁺ are generated by electron transfer between the Co²⁺(tartrate) and the electrode, i.e. directly at the electrode surface.

We will first focus on reactions (**1b**) and (**2**). They are both strongly displaced to the right since the OH⁻ concentration is at least 10³ larger than the Co²⁺ concentration in the solution under our deposition conditions. The crossover from Co₃O₄ to CoOOH deposition with increasing OH⁻ concentration cannot be explained simply by the solution pH. We may thus reasonably consider that the rate of these reactions is limited by the concentration of

$\text{Co}^{2+}(\text{tartrate})$ and Co^{3+} in the vicinity of the electrode surface, determining the deposited phase. For instance, in order to favor reaction (2) and deposit CoOOH , the $\text{Co}^{2+}(\text{tartrate})$ concentration in the vicinity of the electrode should be significantly reduced. This happens when reaction (1a) is fast enough to deplete most of $\text{Co}^{2+}(\text{tartrate})$ close to the electrode surface. This would be one explanation for the formation of CoOOH when the $\text{Co}^{2+}(\text{tartrate})$ bulk concentration is as low as 0.1 mM as shown in **Fig. 5**. In these conditions, the rate of reaction (1a) is limited by $\text{Co}^{2+}(\text{tartrate})$ diffusion from the solution bulk to the electrode. In 1 mM $\text{Co}(\text{NO}_3)_2$, and 1 M NaOH, diffusion limitation seems to play a minor role since we observe Co_3O_4 formation. A means to favour reaction (2) is to slow down the $\text{Co}^{2+}(\text{tartrate})$ diffusion by increasing the solution viscosity, the diffusion coefficient being inversely proportional to the viscosity (Stokes-Einstein relation). Since at 100°C, the viscosity of the 5 M NaOH solution is about 2 times larger than that of a 1 M NaOH solution [34], the diffusion coefficient of $\text{Co}^{2+}(\text{tartrate})$ species is two times smaller in 5 M NaOH. This may be one explanation for the formation of CoOOH in 5 M NaOH and 1 mM $\text{Co}(\text{NO}_3)_2$. The parallel formation of both phases in 2 M NaOH requires that the appropriate growth conditions for both phases are fulfilled, which should only be possible within a narrow parameter range. If we assume that the oxide phase growth is ruled by diffusion, the diffusion conditions should be at a crossover to form simultaneously Co_3O_4 and CoOOH entities. Another way to rationalize the observations, is that we have two different coordination shells (OH species) around the Co^{3+} species at 1 M and 5 M NaOH and that this contributes to favour the formation of one phase or another. Within such a hypothesis, both types of Co species shells would coexist at 2 M NaOH and each type of Co species would contribute to the growth of the corresponding oxide phase, providing an explanation to the simultaneous deposition of the two phases. Further investigations are required to clarify this point.

In the following, we discuss the nucleation and growth modes of both oxides. The structural results demonstrate that crystalline single phase $\text{Co}_3\text{O}_4(111)$ and $\text{CoOOH}(001)$ thin films may be electrodeposited in epitaxy with $\text{Au}(111)$ (**Figs. 1-2**). The nucleation of Co_3O_4 is progressive as suggested by the wide distribution of island sizes in the early stages of growth (see analysis in **Fig. S4**). The nucleation seems to be homogeneous on the $\text{Au}(111)$ surface, in contrast to Co_3O_4 growth on $\text{Au}(100)$ where growth on the Au step edges seems favoured (**Fig. S2**). Further growth proceeds via merging neighbouring islands into larger ones which accounts for the decrease of the island density. The coalescence of several adjacent islands should give rise to grain boundaries which might be too narrow to be imaged by AFM or SEM. Such grain boundaries have been observed by scanning tunnelling microscopy on thin Co_3O_4 films grown under ultrahigh vacuum conditions [35]. This explains why the lateral coherence length measured by XRD in our previous study [27] is significantly smaller than the lateral island size measured by SEM and AFM [32].

In the case of CoOOH deposition on $\text{Au}(111)$, the nucleation step could not be resolved since the Au surface was almost fully covered even at the lowest studied coverage (**Fig. 4d**). The morphology of this very thin CoOOH film is reminiscent of that of the Au substrate and suggests a layer-by-layer growth. The pyramidal growth takes place subsequently (**Fig. 4f**) and the analysis of the pyramid height suggests that they are formed on top of a quasi-2D CoOOH layer which is at least few nm thick. The regularly spaced atomic steps (**Figs. 3b-4e**) is generally associated with a growth mechanism where the building blocks coming from the electrolyte attach preferentially at the substrate steps. The fact that the observed terrace width remains approximatively constant with the deposition time implies that the step growth rate is similar for all steps. In such a continuous step growth, the size of the CoOOH terraces at the top of the pyramids would increase with time yielding pyramids with a large flat top, unless a screw dislocation is present. In **Fig. S3a-b** we give evidence for such

dislocations on the top of the pyramids which act as constant nucleation centers and allow maintaining the pyramid shape during the entire growth process [36]. When these dislocations are absent (**Fig. S3c-d**), the pyramid shape may be maintained if continuous nucleation of a new terrace at its top takes place with a constant nucleation rate. This may occur by homogeneous nucleation of a new CoOOH layer via formation of a critical nucleus on the topmost terrace.

The difference between the nucleation and growth modes of Co_3O_4 and CoOOH is striking, which may be related to the differences in lattice structure. Co oxyhydroxide is a layered oxide, in which hexagonal-packed CoOOH layers are bound only weakly by H bonds along the [001] direction. Due to this anisotropy, a preference for layer-by-layer growth of CoOOH(001) may be expected. In contrast, the Co_3O_4 spinel lattice is a three-dimensional structure. Although its (111) surface is close-packed and thus may be energetically preferred, Co_3O_4 consists along the (111) direction of alternating buckled Co oxide planes composed of $\text{Co}^{2+}/\text{Co}^{3+}$ and pure Co^{3+} , respectively, with similar strong in-plane and out-of-plane Co-O bonds. Another possible reason may be the growth steps at the molecular level. In CoOOH, all Co atoms are Co^{3+} and occupy equivalent octahedral sites. Consequently, any surface site can accept an additional Co^{3+} species generated by reaction (**1a**). In contrast, Co_3O_4 contains Co^{2+} and Co^{3+} occupying tetrahedral and octahedral sites respectively at specific positions in the lattice. Growing Co_3O_4 thus requires either the incorporation of Co^{2+} and Co^{3+} species diffusing to specific lattice positions or charge transfer between adjacent Co atoms in the lattice and rearrangement of the local environment to maintain the long range order. These growth steps which are absent in the case of CoOOH may contribute to the different growth mode and larger surface roughness of Co_3O_4 .

5. Conclusion

We have demonstrated the preparation of $\text{Co}_3\text{O}_4(111)$ and $\text{CoOOH}(001)$ epitaxial films on $\text{Au}(111)$ that exhibit well-defined morphology and full surface coverage. The obtained phase may be controlled by fine tuning the deposition conditions. The growth behaviour of the two oxides is different. CoOOH films grow layer-by-layer and form wide shallow pyramids with stepped facets partly due to the presence of screw dislocations. This leads to ideally flat CoOOH films. Co_3O_4 films grow three-dimensionally after progressive nucleation. This yields compact granular Co_3O_4 films with flat top islands. The flatness of the spinel film is improved if deposition is conducted on a CoOOH buffer layer. These $\text{Co}_3\text{O}_4(111)$ and $\text{CoOOH}(001)$ epitaxial films with well-defined surfaces morphology can be employed as model catalysts for operando studies to gain insight into the OER mechanism on these oxides.

Acknowledgments:

This work is supported by a public grant from the French National Research Agency (ANR): EC+MEC ANR-16-CE24-0018-04 and the Deutsche Forschungsgemeinschaft (DFG) via project number 284207613 and SFB/TRR247 (project number 388390466).

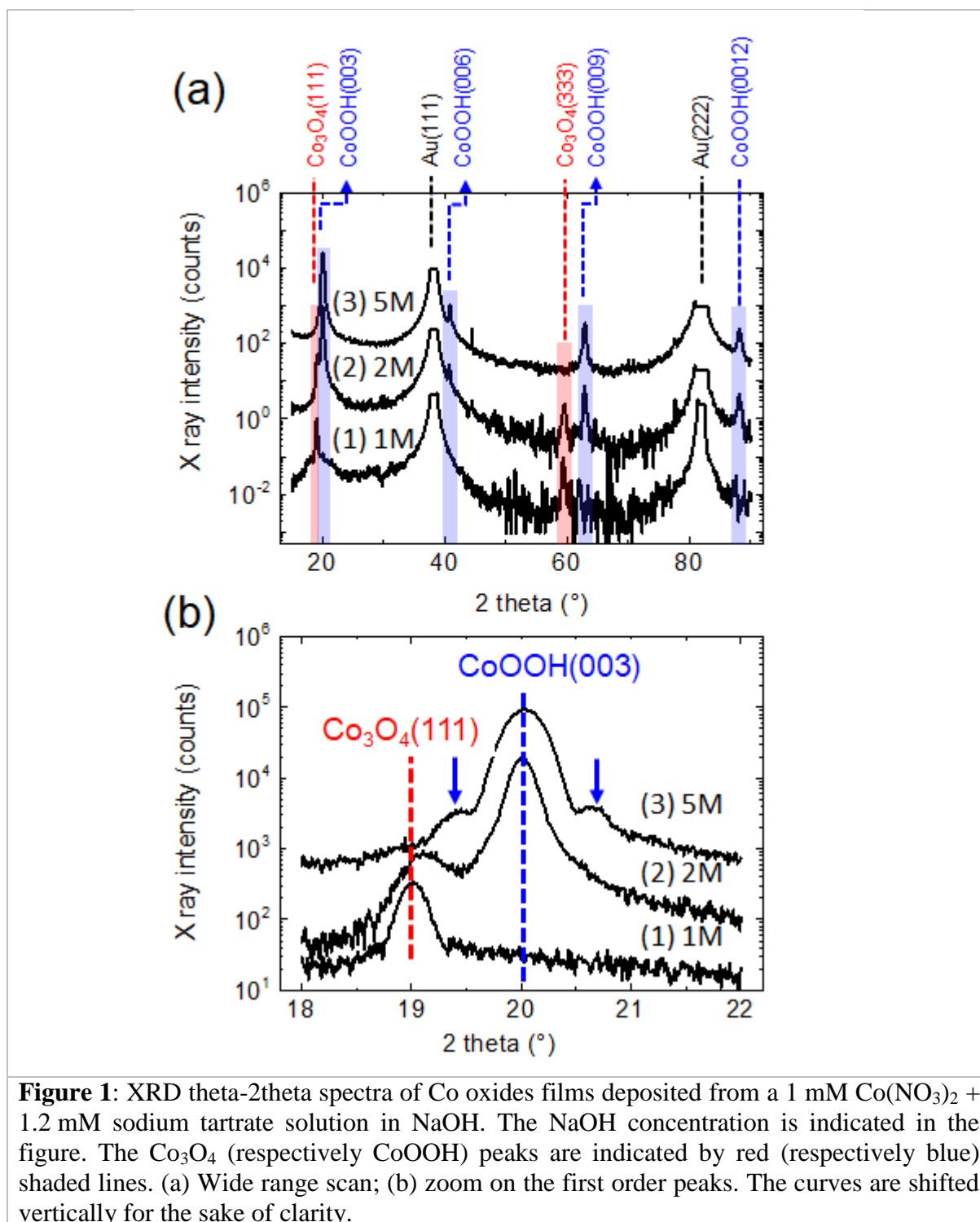
References:

- ¹ S. Trasatti, Electrocatalysis in the anodic evolution of oxygen and chlorine *Electrochim. Acta* **29** (11), 1503 (1984).
- ² I. C. Man, H.-Y. Su, F. Calle-Vallejo, H. A. Hansen, J. I. Martínez, N. G. Inoglu, J. Kitchin, T. F. Jaramillo, J. K. Nørskov, and J. Rossmeisl, Universality in Oxygen Evolution Electrocatalysis on Oxide Surfaces *ChemCatChem* **3** (7), 1159 (2011).
- ³ X. Deng and H. Tüysüz, Cobalt-Oxide-Based Materials as Water Oxidation Catalyst: Recent Progress and Challenges *ACS Catalysis* **4** (10), 3701 (2014).
- ⁴ N.-T. Suen, S.-F. Hung, Q. Quan, N. Zhang, Y.-J. Xu, and H. M. Chen, Electrocatalysis for the oxygen evolution reaction: recent development and future perspectives *Chemical Society Reviews* **46** (2), 337 (2017).
- ⁵ C. C. L. McCrory, S. Jung, I. M. Ferrer, S. M. Chatman, J. C. Peters, and T. F. Jaramillo, Benchmarking Hydrogen Evolving Reaction and Oxygen Evolving Reaction Electrocatalysts for Solar Water Splitting Devices *Journal of the American Chemical Society* **137** (13), 4347 (2015).
- ⁶ M. S. Burke, S. Zou, L. J. Enman, J. E. Kellon, C. A. Gabor, E. Pledger, and S. W. Boettcher, Revised Oxygen Evolution Reaction Activity Trends for First-Row Transition-Metal (Oxy)hydroxides in Alkaline Media *The Journal of Physical Chemistry Letters* **6** (18), 3737 (2015).
- ⁷ R. L. Doyle, I. J. Godwin, M. P. Brandon, and M. E. G. Lyons, Redox and electrochemical water splitting catalytic properties of hydrated metal oxide modified electrodes *Phys. Chem. Chem. Phys.* **15** (33), 13737 (2013).
- ⁸ F. Song, L. Bai, A. Moysiadou, S. Lee, C. Hu, L. Liardet, and X. Hu, Transition Metal Oxides as Electrocatalysts for the Oxygen Evolution Reaction in Alkaline Solutions: An Application-Inspired Renaissance *Journal of the American Chemical Society* **140** (25), 7748 (2018).
- ⁹ J. Song, C. Wei, Z.-F. Huang, C. Liu, L. Zeng, X. Wang, and Z. J. Xu, A review on fundamentals for designing oxygen evolution electrocatalysts *Chemical Society Reviews* **49** (7), 2196 (2020).
- ¹⁰ V. Artero, M. Chavarot-Kerlidou, and M. Fontecave, Splitting Water with Cobalt *Angewandte Chemie International Edition* **50** (32), 7238 (2011).
- ¹¹ C. Pirovano and S. Trasatti, The point of zero charge of Co₃O₄: Effect of the preparation procedure *Journal of Electroanalytical Chemistry and Interfacial Electrochemistry* **180** (1), 171 (1984).

- ¹² D. Yuming, H. Kun, Y. Lin, and Z. Aimin, A facile route to controlled synthesis of Co₃O₄ nanoparticles and their environmental catalytic properties *Nanotechnology* **18** (43), 435602 (2007).
- ¹³ A. Bergmann, E. Martinez-Moreno, D. Teschner, P. Chernev, M. Gliech, J. F. de Araújo, T. Reier, H. Dau, and P. Strasser, Reversible amorphization and the catalytically active state of crystalline Co₃O₄ during oxygen evolution *Nature Communications* **6**, 8625 (2015).
- ¹⁴ E. Hosono, S. Fujihara, I. Honma, M. Ichihara, and H. Zhou, Synthesis of the CoOOH fine nanoflake film with the high rate capacitance property *Journal of Power Sources* **158** (1), 779 (2006).
- ¹⁵ A. J. Esswein, M. J. McMurdo, P. N. Ross, A. T. Bell, and T. D. Tilley, Size-Dependent Activity of Co₃O₄ Nanoparticle Anodes for Alkaline Water Electrolysis *The Journal of Physical Chemistry C* **113** (33), 15068 (2009).
- ¹⁶ C. M. Hull, J. A. Koza, and J. A. Switzer, Electrodeposition of epitaxial Co(OH)₂ on gold and conversion to epitaxial CoOOH and Co₃O₄ *J. Mater. Res.* **31** (21), 3324 (2016).
- ¹⁷ D. Friebel, M. Bajdich, B. S. Yeo, M. W. Louie, D. J. Miller, H. Sanchez Casalongue, F. Mbuga, T.-C. Weng, D. Nordlund, D. Sokaras, R. Alonso-Mori, A. T. Bell, and A. Nilsson, On the chemical state of Co oxide electrocatalysts during alkaline water splitting *Phys. Chem. Chem. Phys.* **15** (40), 17460 (2013).
- ¹⁸ J. A. Koza, Z. He, A. S. Miller, and J. A. Switzer, Electrodeposition of Crystalline Co₃O₄—A Catalyst for the Oxygen Evolution Reaction *Chem. Mat.* **24** (18), 3567 (2012).
- ¹⁹ T. Pauporté, L. Mendoza, M. Cassir, M. C. Bernard, and J. Chivot, Direct Low-Temperature Deposition of Crystallized CoOOH Films by Potentiostatic Electrolysis *J. Electrochem. Soc.* **152** (2), C49 (2005).
- ²⁰ A. D. Jagdale, D. P. Dubal, and C. D. Lokhande, Electrochemical behavior of potentiodynamically deposited cobalt oxyhydroxide (CoOOH) thin films for supercapacitor application *Materials Research Bulletin* **47** (3), 672 (2012).
- ²¹ M. Mathankumar, S. Anantharaj, A. K. Nandakumar, S. Kundu, and B. Subramanian, Potentiostatic phase formation of β-CoOOH on pulsed laser deposited biphasic cobalt oxide thin film for enhanced oxygen evolution *Journal of Materials Chemistry A* **5** (44), 23053 (2017).
- ²² M. W. Kanan and D. G. Nocera, In Situ Formation of an Oxygen-Evolving Catalyst in Neutral Water Containing Phosphate and Co²⁺ *Science* **321** (5892), 1072 (2008).
- ²³ Y. Surendranath, M. Dincă, and D. G. Nocera, Electrolyte-Dependent Electrosynthesis and Activity of Cobalt-Based Water Oxidation Catalysts *Journal of the American Chemical Society* **131** (7), 2615 (2009).
- ²⁴ M. Risch, F. Ringleb, M. Kohlhoff, P. Bogdanoff, P. Chernev, I. Zaharieva, and H. Dau, Water oxidation by amorphous cobalt-based oxides: in situ tracking of redox transitions and mode of catalysis *Energy & Environmental Science* **8** (2), 661 (2015).
- ²⁵ A. R. Akbashev, Electrocatalysis Goes Nuts *ACS Catalysis* **12** (8), 4296 (2022).
- ²⁶ C. Wei, R. R. Rao, J. Peng, B. Huang, I. E. L. Stephens, M. Risch, Z. J. Xu, and Y. Shao-Horn, Recommended Practices and Benchmark Activity for Hydrogen and Oxygen Electrocatalysis in Water Splitting and Fuel Cells *Adv. Mater.* **31** (31), 1806296 (2019).
- ²⁷ F. Reikowski, F. Maroun, I. Pacheco, T. Wiegmann, P. Allongue, J. Stettner, and O. M. Magnussen, Operando Surface X-ray Diffraction Studies of Structurally Defined Co₃O₄ and CoOOH Thin Films during Oxygen Evolution *ACS Catalysis* **9**, 3811 (2019).
- ²⁸ D. Grumelli, T. Wiegmann, S. Barja, F. Reikowski, F. Maroun, P. Allongue, J. Balajka, G. S. Parkinson, U. Diebold, K. Kern, and O. M. Magnussen, Electrochemical Stability of the Reconstructed Fe₃O₄(001) Surface *Angewandte Chemie International Edition* **n/a** (n/a).

- ²⁹ J. Fester, A. Makoveev, D. Grumelli, R. Gutzler, Z. Sun, J. Rodríguez-Fernández, K. Kern, and J. V. Lauritsen, The Structure of the Cobalt Oxide/Au Catalyst Interface in Electrochemical Water Splitting *Angewandte Chemie International Edition* **57** (37), 11893 (2018).
- ³⁰ F. Faisal, M. Bertram, C. Stumm, S. Cherevko, S. Geiger, O. Kasian, Y. Lykhach, O. Lytken, K. J. J. Mayrhofer, O. Brummel, and J. Libuda, Atomically Defined Co₃O₄(111) Thin Films Prepared in Ultrahigh Vacuum: Stability under Electrochemical Conditions *The Journal of Physical Chemistry C* **122** (13), 7236 (2018).
- ³¹ J. Fester, A. Walton, Z. Li, and J. V. Lauritsen, Gold-supported two-dimensional cobalt oxyhydroxide (CoOOH) and multilayer cobalt oxide islands *Phys. Chem. Chem. Phys.* **19** (3), 2425 (2017).
- ³² T. Wiegmann, I. Pacheco, F. Reikowski, J. Stettner, C. Qiu, M. Bouvier, M. Bertram, F. Faisal, O. Brummel, J. Libuda, J. Drnec, P. Allongue, F. Maroun, and O. M. Magnussen, Operando Identification of the Reversible Skin Layer on Co₃O₄ as a Three-Dimensional Reaction Zone for Oxygen Evolution *ACS Catalysis* **12** (6), 3256 (2022).
- ³³ A. Guinier, *Théorie et technique de la radiocristallographie*. (Dunod, Paris, 1964).
- ³⁴ D. Le Bideau, P. Mandin, M. Benbouzid, M. Kim, and M. Sellier, Review of necessary thermophysical properties and their sensitivities with temperature and electrolyte mass fractions for alkaline water electrolysis multiphysics modelling *International Journal of Hydrogen Energy* **44** (10), 4553 (2019).
- ³⁵ W. Meyer, K. Biedermann, M. Gubo, L. Hammer, and K. Heinz, Surface structure of polar Co₃O₄(111) films grown epitaxially on Ir(100)-(1 × 1) *Journal of Physics: Condensed Matter* **20** (26), 265011 (2008).
- ³⁶ F. Meng, S. A. Morin, A. Forticaux, and S. Jin, Screw Dislocation Driven Growth of Nanomaterials *Accounts of Chemical Research* **46** (7), 1616 (2013).

Figures



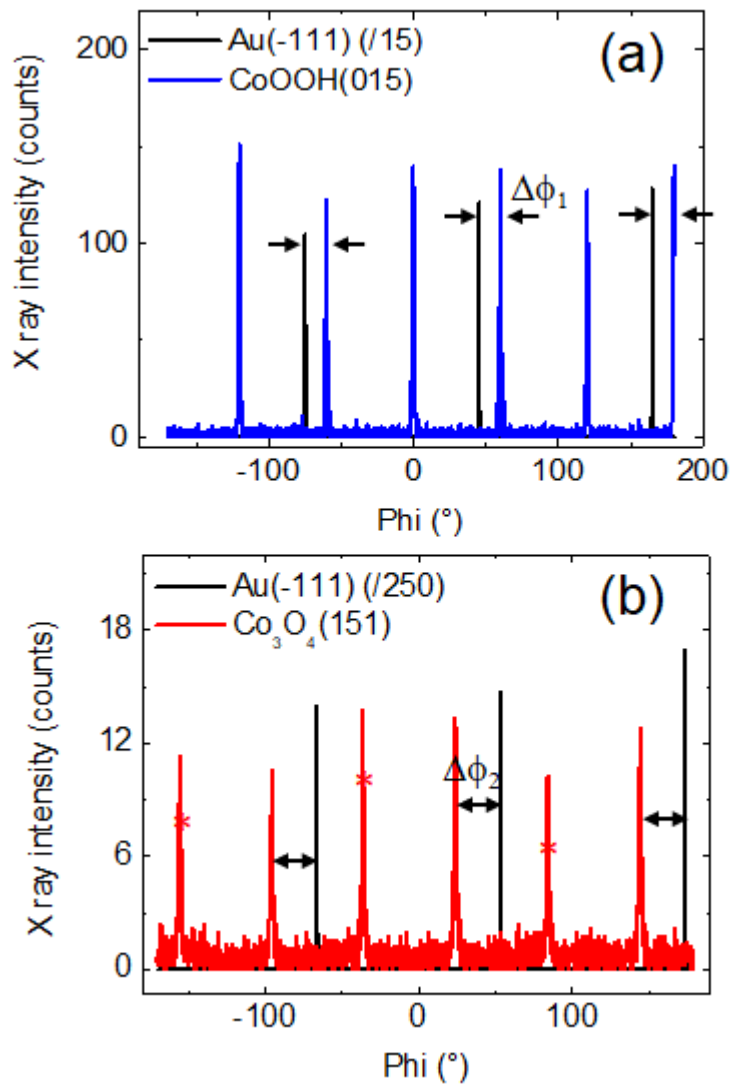


Figure 2: Phi scans at the Bragg positions of CoOOH(015) peaks (a, red curve) and $\text{Co}_3\text{O}_4(151)$ peaks (b, red curve). In each plot the same scan of Au(-111) peaks is shown in black. The phi separation between the Co oxide peaks and that of Au is indicated by arrows and named $\Delta\Phi_1$ (CoOOH) and $\Delta\Phi_2$ (Co_3O_4)

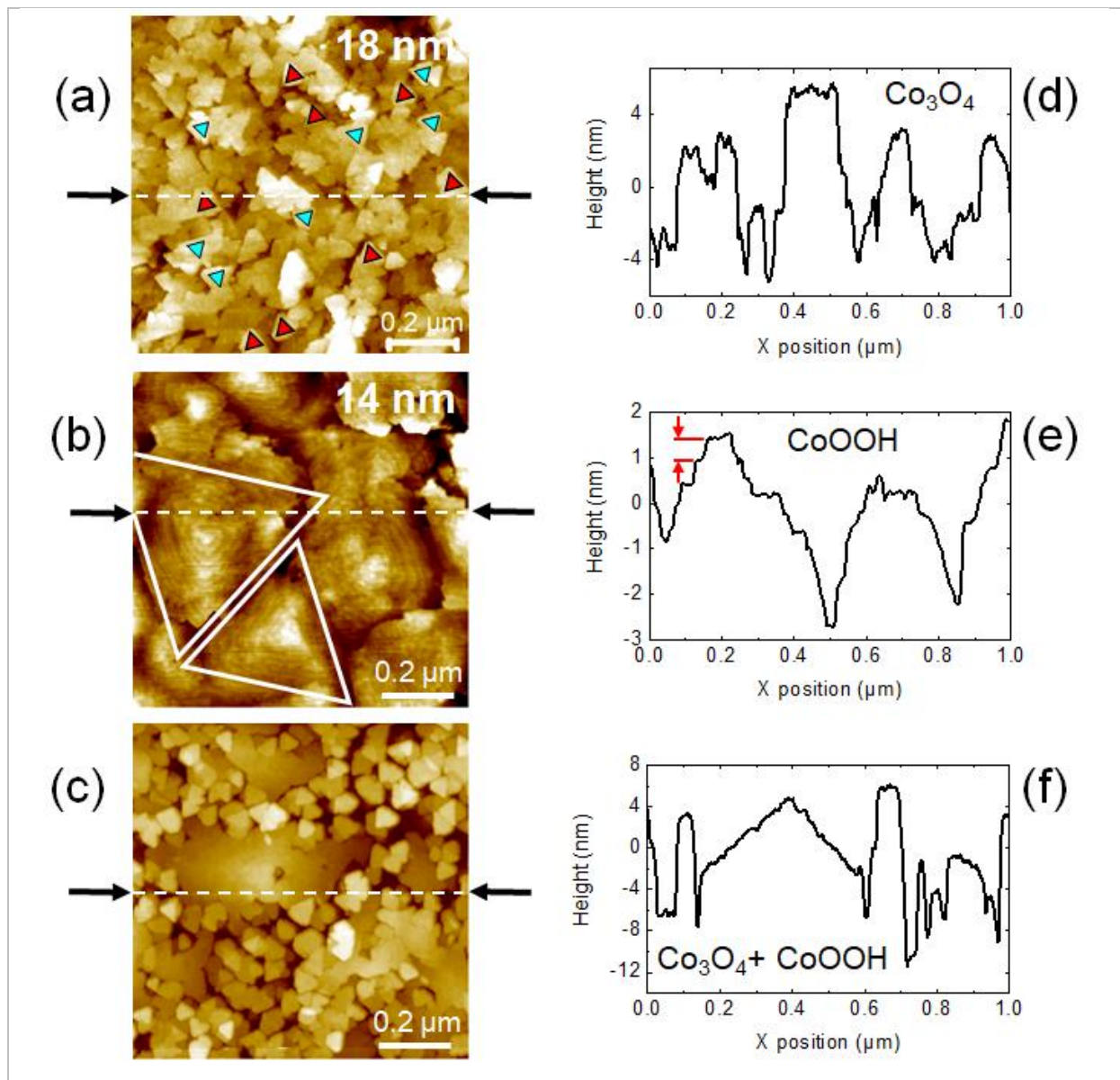


Figure 3: AFM images and height profiles of Co oxides grown from a 1 mM $\text{Co}(\text{NO}_3)_2$ + 1.2 mM sodium tartrate solution in 1 M NaOH (a and d), 5 M NaOH (b and e) and 2 M NaOH (c and f). The film thickness d_{av} is indicated on the top right corner of images. The height profiles are horizontal and their position is indicated by black arrows and dashed white lines in each image. The blue and red triangles in (a) and (b) highlight Co oxide grains with different in-plane orientations. The red arrows in (e) indicate the height of a CoOOH atomic step.

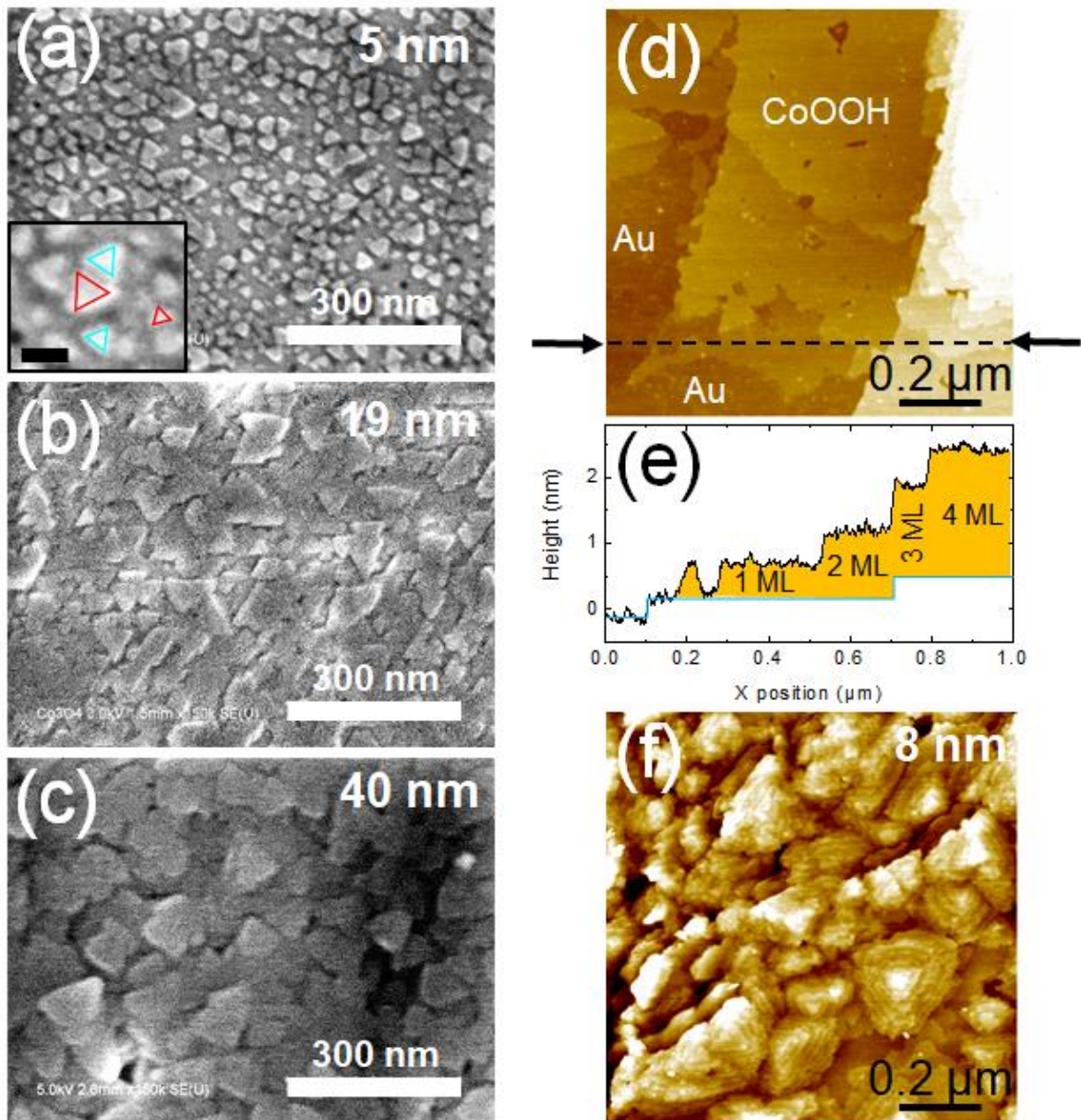


Figure 4: (a, b and c) SEM images of Co_3O_4 films grown from a 1 mM $\text{Co}(\text{NO}_3)_2$ + 1.2 mM sodium tartrate solution in 1 M NaOH at different growth stages with d_{av} varying from 5 to 40 nm. The inset in (a) shows an enlarged section of the same image. The scale bar in the inset corresponds to 30 nm. (d and f) AFM images of CoOOH films grown from a 1 mM $\text{Co}(\text{NO}_3)_2$ + 1.2 mM sodium tartrate solution in 5 M NaOH at different growth stages. (e) is a horizontal height profile from d indicated by black arrows and dashed line. The blue line indicates the Au step morphology and the numbers 1-4 ML give the local CoOOH thickness.

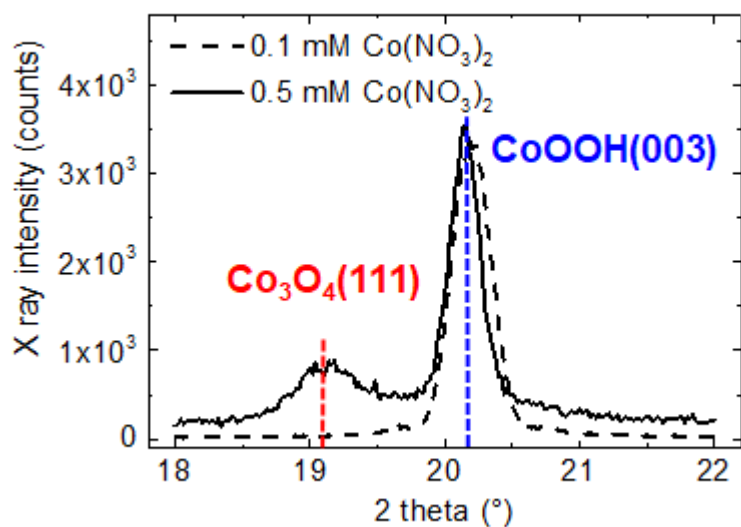


Figure 5: XRD theta-2theta scans of Co oxide films deposited from a $\text{Co}(\text{NO}_3)_2$ + sodium tartrate solution in 1 M NaOH at -0.55 V. The $\text{Co}(\text{NO}_3)_2$ concentration is 0.5 mM (solid curve) and 0.1 mM (dashed curve). The sodium tartrate concentration is always 1.2 times that of $\text{Co}(\text{NO}_3)_2$. $\text{Co}_3\text{O}_4(111)$ and $\text{CoOOH}(003)$ peaks are indicated by blue and red dashed lines respectively.

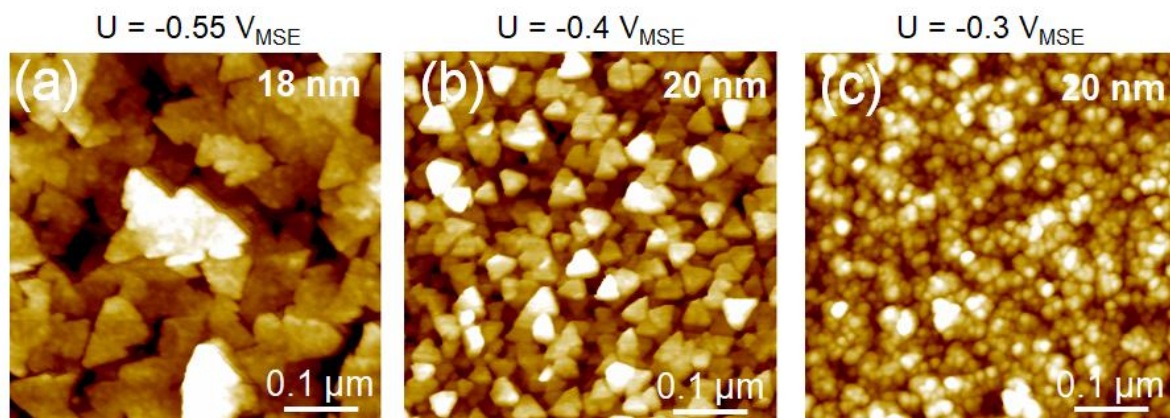
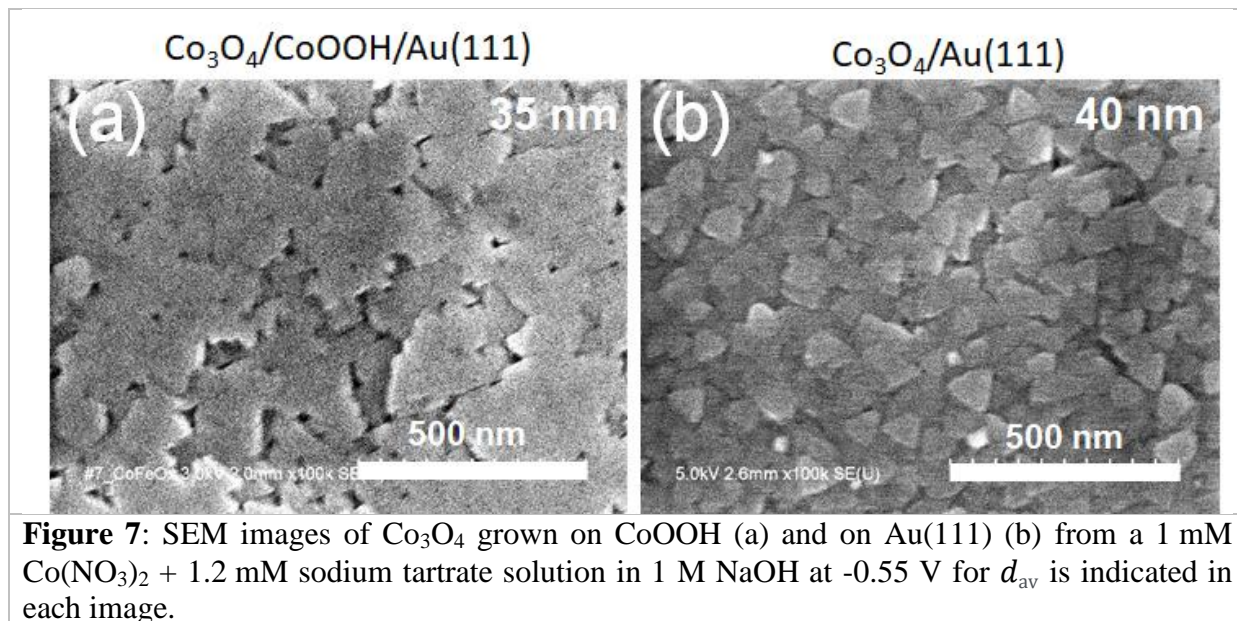


Figure 6: AFM images of Co_3O_4 deposited at different potentials from a 1 mM $\text{Co}(\text{NO}_3)_2$ + 1.2 mM sodium tartrate solution in 1 M NaOH: -0.55 V (a), -0.4 V (b) and -0.3 V (c). d_{av} is indicated in each image.



Supplementary information:

Growth of ultrathin well-defined and crystalline films of Co_3O_4 and CoOOH by electrodeposition

I. Pacheco¹, M. Bouvier¹, O. M. Magnussen^{2*}, P. Allongue^{1*}, F. Maroun^{1*}

¹ Laboratoire de Physique de la Matière Condensée (PMC), CNRS, Ecole Polytechnique, Institut Polytechnique de Paris, 91120 Palaiseau, France

² Institut für Experimentelle und Angewandte Physik, Christian-Albrechts-Universität zu Kiel, Kiel, Germany.

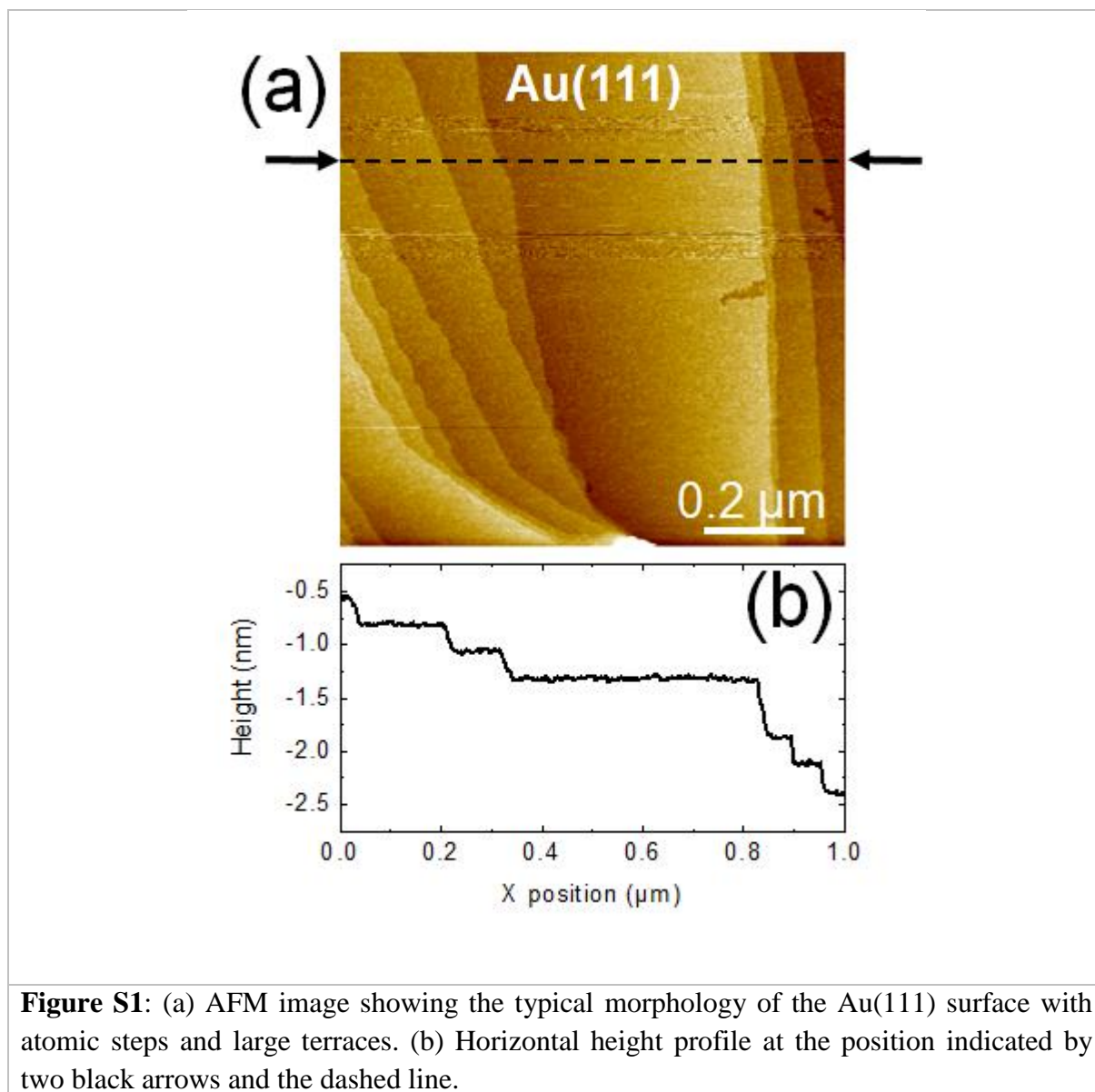
* *corresponding authors:*

fouad.maroun@polytechnique.edu, philippe.allongue@polytechnique.edu,
magnussen@physik.uni-kiel.de

Content:

- 1) Surface morphology of the Au(111) substrate
- 2) Morphology of Co_3O_4 on Au(100)
- 3) Topography of the CoOOH pyramids on Au(111)
- 4) Lateral size distribution of $\text{Co}_3\text{O}_4/\text{Au}(111)$ films
- 5) Morphology of CoOOH film on Au(111)
- 6) XRD spectra of the two step growth of $\text{Co}_3\text{O}_4/\text{CoOOH}/\text{Au}(111)$ films
- 7) Analysis of the Bragg peak FWHM

1. Surface morphology of the Au(111) substrate:



2. Morphology of Co_3O_4 on Au(100):

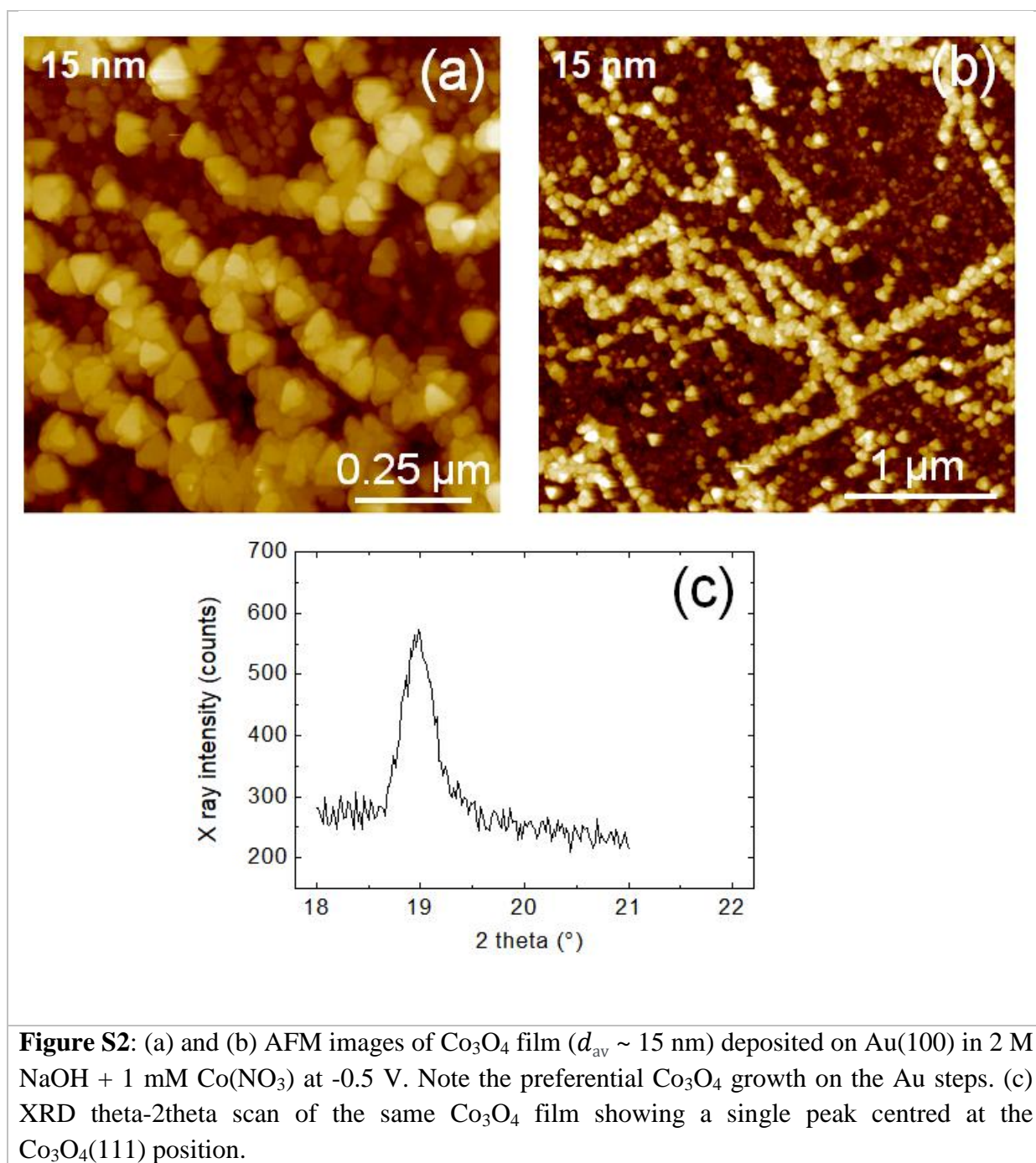


Figure S2: (a) and (b) AFM images of Co_3O_4 film ($d_{av} \sim 15$ nm) deposited on Au(100) in 2 M NaOH + 1 mM $\text{Co}(\text{NO}_3)_2$ at -0.5 V. Note the preferential Co_3O_4 growth on the Au steps. (c) XRD theta-2theta scan of the same Co_3O_4 film showing a single peak centred at the $\text{Co}_3\text{O}_4(111)$ position.

3. Topography of the CoOOH pyramids on Au(111):

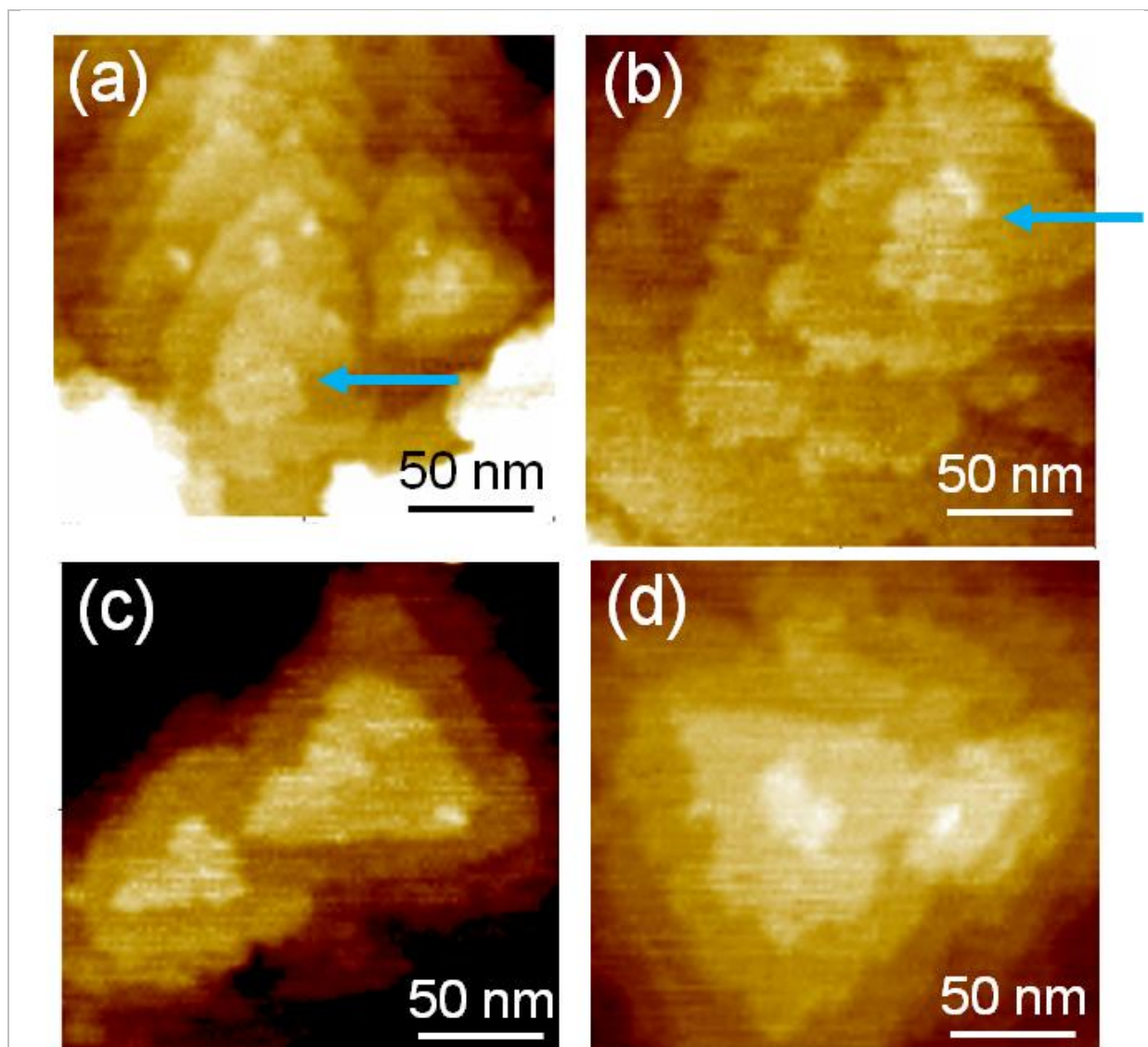
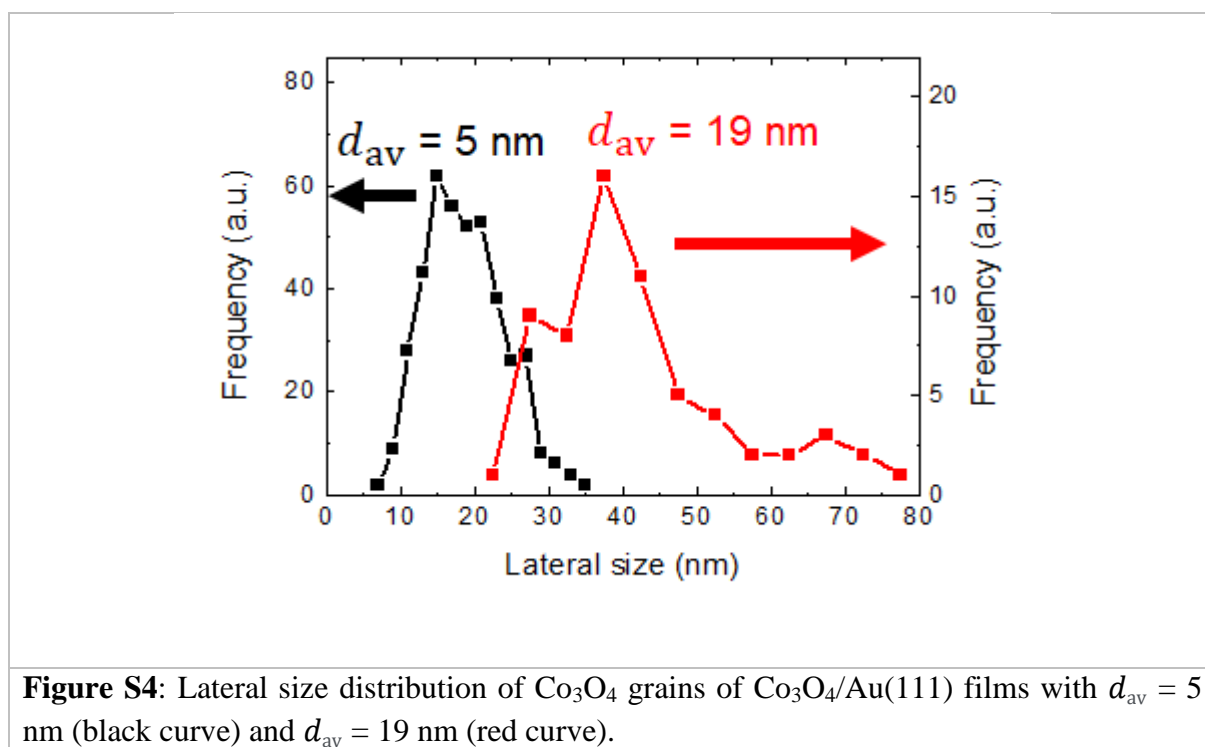
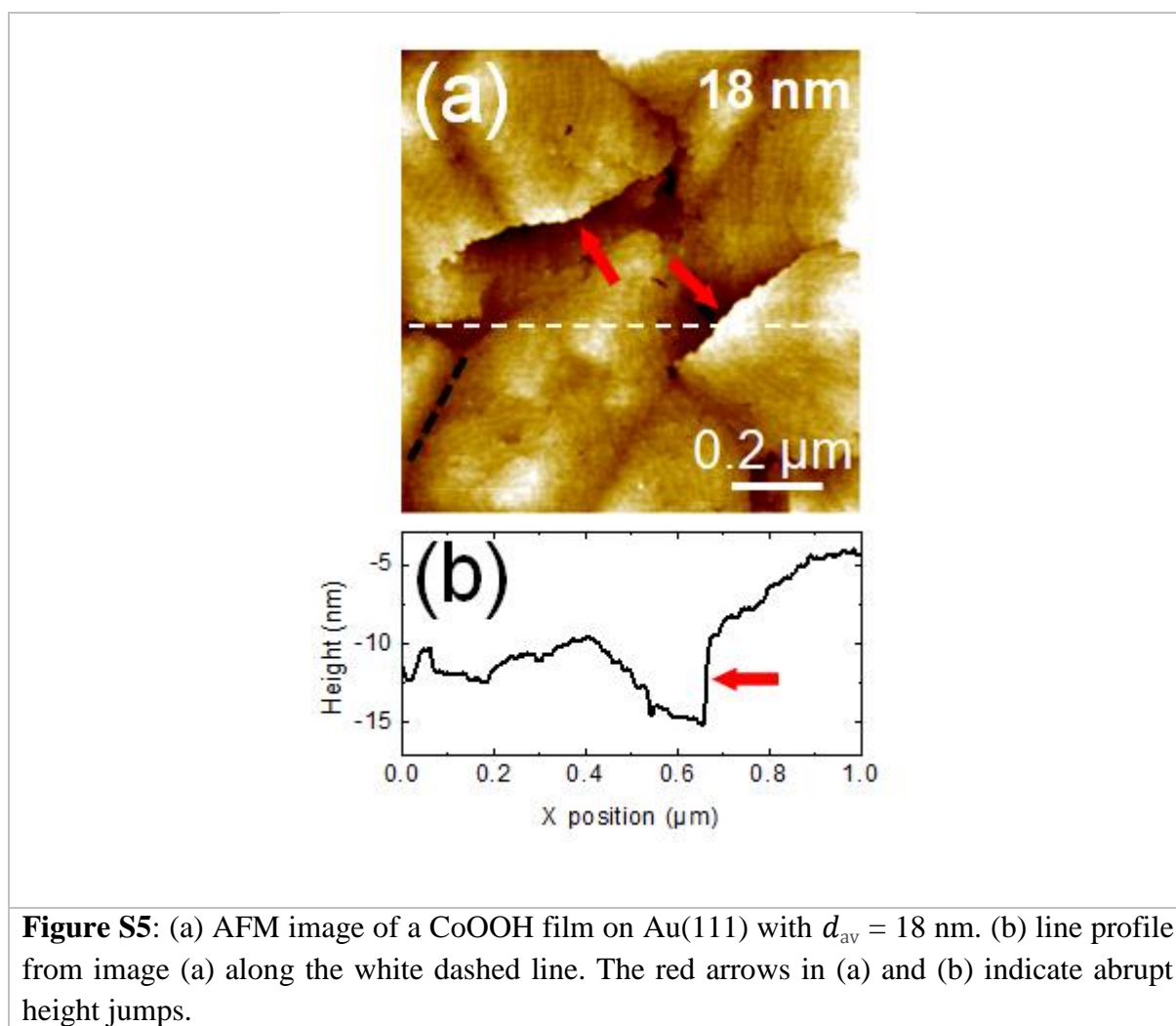


Figure S3: AFM images zoomed on the top of several CoOOH pyramids. (a) and (b) in each image, one screw dislocation is located in the centre of the topmost CoOOH plane and is indicated by a blue arrow. In images (c) and (d), no screw dislocation could be observed and the pyramid top is terminated by a small terrace.

4. Lateral size distribution of Co_3O_4 grains on Au(111):



5. Morphology of CoOOH film on Au(111):



6. XRD spectra of the two step growth of $\text{Co}_3\text{O}_4/\text{CoOOH}/\text{Au}(111)$ films:

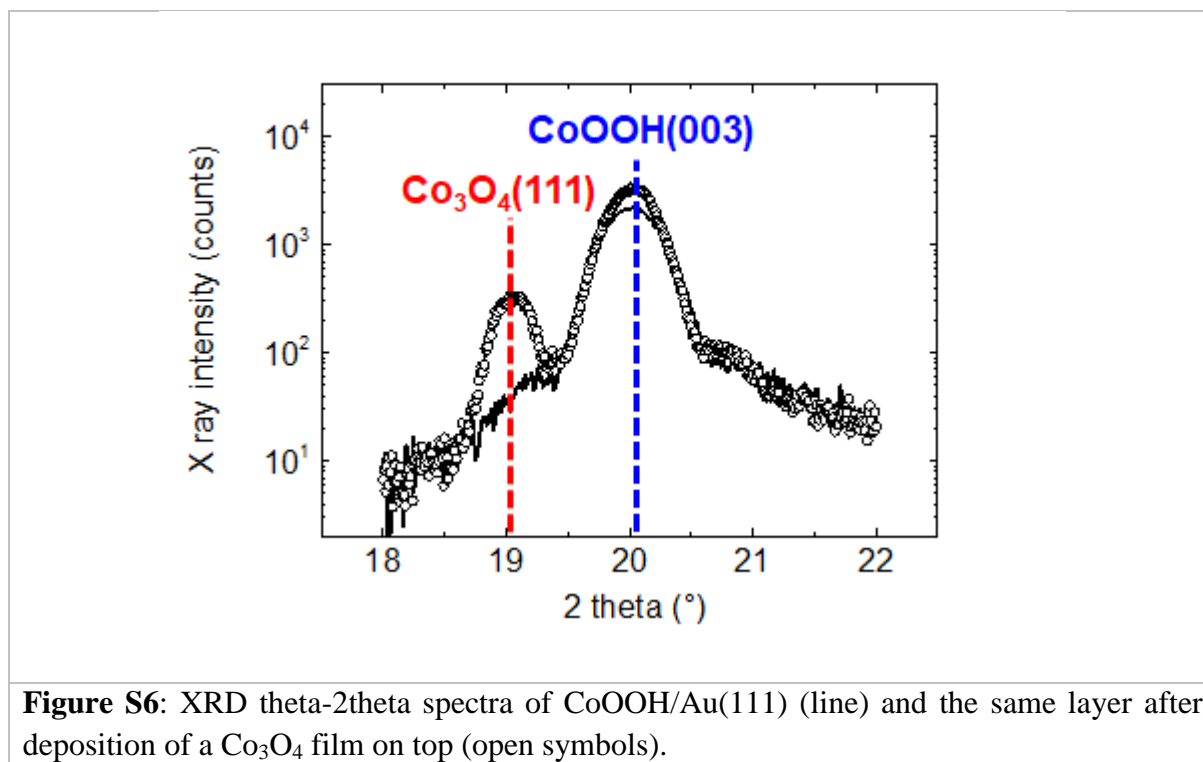


Figure S6: XRD theta-2theta spectra of CoOOH/Au(111) (line) and the same layer after deposition of a Co_3O_4 film on top (open symbols).

7. Analysis of the Bragg peak FWHM:

We saw that the FWHM of Co_3O_4 and CoOOH peaks in the phi scans is significantly larger than that of the Au substrate which suggests that it is not due to instrumental limitations. This peak broadening may originate from the in-plane finite size of the crystallites, the in-plane angular distribution of the crystallites around the preferred orientations or the measurement conditions. We will discuss the latter first. In these phi scans, the Ewald sphere is fixed and the detector at a position where the Bragg peak is expected. The effect of moving phi is to rotate the entire sample reciprocal space to make the Bragg reflections intersect the Ewald sphere and be measured by the detector. The FWHM of the peak in the phi scan may thus be seen as the phi range necessary for the Bragg peak to cross entirely the Ewald sphere at the detector position. This depends not only on the diffraction spot size but also on the detector height (H) and increases as $1/\cos(H)$. Therefore, for comparing the FWHM of phi scan peaks,

one needs to take into account this correction. Considering the H values of $\text{Co}_3\text{O}_4(151)$, $\text{CoOOH}(015)$ and $\text{Au}(-111)$ of $H_{\text{Co}_3\text{O}_4} = 49.8^\circ$, $H_{\text{CoOOH}} = 35.6^\circ$ and $H_{\text{Au}} = 12.5^\circ$ respectively, the corrected FWHM would be 1.23° , 1.14° and 0.39° for Co_3O_4 , CoOOH and Au respectively. This correction brings the values of both oxide phases close to each other but they remain significantly larger than that of Au . The remaining broadening may then be attributed to the other two mentioned origins, the lateral size or the in-plane rotation of the crystallites. If the broadening is due to the in-plane size, this would yield crystallites of a lateral size smaller than 10 nm which is not consistent with former studies where lateral sizes larger than 20 nm were found (Reikowski ACS catalysis). We then conclude that this broadening of $\sim 1^\circ$ is mainly due to the in-plane rotation of the crystallites around their preferred orientations.